Journal of Power Sources 553 (2023) 232302

Contents lists available at ScienceDirect

Journal of Power Sources

journal homepage: www.elsevier.com/locate/jpowsour

Structure dependence of fracture toughness and ionic conductivity in lithium borophosphate glassy electrolytes for all-solid-state batteries

Zhimin Chen [a,1], Tao Du [a,1], Søren S. Sørensen [a], Rasmus Christensen [a], Qi Zhang [a], Lars R. Jensen [b], Oxana V. Magdysyuk [c], Maria Diaz-Lopez [c], Mathieu Bauchy [d], Yuanzheng Yue [a], Morten M. Smedskjaer [a,*]

[a] Department of Chemistry and Bioscience, Aalborg University, Aalborg East, 9220, Denmark
[b] Department of Materials and Production, Aalborg University, Aalborg East, 9220, Denmark
[c] Diamond Light Source Ltd., Harwell Science and Innovation Campus, Didcot, OX11 0DE, UK
[d] Department of Civil and Environmental Engineering, University of California, Los Angeles, CA, 90095, USA

HIGHLIGHTS

- Structures of Li_2O–B_2O_3–P_2O_5 glassy electrolytes are reproduced by MD simulations.
- Composition dependence of mechanical properties is shown by experiments and MD.
- Fracture energy can be dissipated through stress-driven conversion of BO_4 to BO_3.
- Hopping of lithium ions between superstructural rings facilitates ionic conduction.

GRAPHICAL ABSTRACT

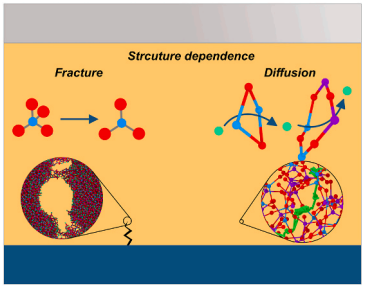

ABSTRACT

Glass materials are potential candidates as solid electrolytes for batteries, but the atomistic origins of the variations in their properties and functionalities with composition are not well understood. Here, based on combined experimental and simulation techniques, we investigate the structural origin of the variation in fracture toughness and ionic conductivity of lithium borophosphate glass electrolytes with varying compositions. We focus on these properties since they are critically important for mechanical stability and electrochemical performances of glassy electrolytes. To this end, we have performed molecular dynamics simulations combined with X-ray total scattering experiments to provide the atomic picture of the disordered structure of borophosphate glass. The mechanical properties have been characterized through single-edge precracked beam measurements and axial tensile simulations. We find that the deformation and fracture behaviors of the electrolytes are governed by bond switching events of boron, which dissipate the strain energy during fracture. The migration of lithium ions in the electrolyte network is facilitated by hopping between superstructural rings, which reflects the important role of medium-range order structure in determining the lithium-ion diffusion. These findings have important implications for the design of future glassy electrolytes.

* Corresponding author.
E-mail address: mos@bio.aau.dk (M.M. Smedskjaer).
[1] These authors contributed equally to this work.

https://doi.org/10.1016/j.jpowsour.2022.232302
Received 21 August 2022; Received in revised form 6 October 2022; Accepted 23 October 2022
Available online 3 November 2022

1. Introduction

The development of safe and efficient batteries is one of the key technologies for electrification of transportation and storage of wind and solar energy [1–4]. Among the various batteries designed to store energy, lithium-ion batteries (LIBs) have proven to be an efficient energy storage system in terms of energy and power density, reliability, and cyclability [5–7]. While lithium-ion batteries have revolutionized the portable electronics industry [6,8], large-scale energy storage calls for improvements in battery performance, energy density, and cost [9,10]. Meanwhile, owing to concerns about the safety issue as well as limited energy density of lithium batteries [11], research on LIBs is moving toward all-solid-state lithium batteries, which involve solid electrolytes.

Solid electrolytes feature numerous advantages, such as enhanced safety, increased energy density, solid device integration, and packaging [12], but also a number of challenges that need to be overcome, including the ability of lithium to penetrate the solid material, the stability of interfaces, and the maintenance of physical contact [13]. In particular, the mechanical properties of the solid electrolytes need to be improved to suppress the generation of lithium dendrites and the sensitivity of the interface to stress during electrochemical cycling. Deformation, crack formation, and crack propagation [14] are key mechanical challenges for solid-state electrolytes in complex electrochemical environments. The resistance to crack propagation is defined by the fracture toughness (K_{Ic}), which is indeed a controlling factor for evaluating fracture performance of solid-state battery components [15].

Many of the most promising solid electrolyte materials are partially or completely amorphous [15,16]. The disordered nature of glassy solid electrolytes implies a lack of periodicity in structure and symmetric long-range migration paths [15], but glasses' out-of-equilibrium nature also enables a continuous tuning of the composition and thus properties as well as formability [16]. However, although the mechanical properties of solid electrolytes directly affect real world performance of the battery, they are rarely characterized and poorly understood. Indeed, there are only very few measurements of mechanics of glassy electrolyte materials, although some studies have been done on the crack behavior of electrode materials in lithium batteries [17] and the viscoplastic mechanical behavior of glassy sulfide electrolytes [18]. Due to the lack of crystalline defects that can provide toughening in crystalline electrolytes, the mechanical properties of amorphous electrolytes are particularly important to be understood. The lack of a unified theory for ionic conduction in amorphous electrolytes is another challenge [19,20].

The purpose of this paper is to investigate the mechanical properties and ionic conductivity of a family of glassy electrolytes to provide a first step toward establishing general structure-property relations, which will help future electrolyte design. We here focus on lithium borophosphate (LiBP) glasses because they are relatively chemically stable in air, enabling well-controlled experimental characterization. First, Raman and X-ray total scattering were performed to characterize the structure of the glassy electrolytes, both on the short- and medium-range order length scales. Then, molecular dynamics (MD) simulations were carried out to extract further structural details and enable comparison with the experiments. The mechanical properties and fracture behaviors of the electrolytes were assessed by indentation, single-edge precracked beam (SEPB) method and MD simulations combined with bond switching analysis. Furthermore, the topological features in the atomic structure were analyzed through persistent homology and ring statistics analyses. Clear structure correlations with both fracture toughness and ionic conduction could then be identified.

2. Experimental and computational details

2.1. Sample preparation

Glassy electrolytes with molar composition of xLi$_2$O-(100-x)($0.5B_2O_3$-$0.5P_2O_5$) (with x = 38, 40, 42.5, and 45, labeled as 38LiBP, 40LiBP, 42.5LiBP, and 45LiBP, respectively) were synthesized by the melt-quenching method. These compositions were chosen since their ionic conductivity data have been reported in literature [21], enabling us to compare these data with those from the present MD simulations. Moreover, these compositions exhibit good glass-forming ability [21], meaning that no detectable crystals are present in the samples. This ensures obtaining the pure-glassy electrolytes for the present study.

Lithium carbonate (Li_2CO_3, ≥98.5%, Merck KGaA), boric acid (H_3BO_3, ≥99.5%, Honeywell International), and ammonium dihydrogen phosphate ($NH_4H_2PO_4$, ≥99.5%, Merck KGaA) were used as raw materials for preparing the glasses. Each well-mixed batch was melted in an Al_2O_3 crucible at 900–1000 °C depending on composition for ~1.5 h and then quenched onto a brass plate. The samples were annealed at their glass transition temperature (T_g) for 30 min (the measured T_g values are listed in Table S1). Subsequent X-ray diffraction (Empyrean XRD, PANalytical) analysis confirmed the non-crystalline nature of the samples (see Fig. S1 in Supporting Information), while optical spectroscopy (Cary 50 Bio, Varian) quantified the transparency of the samples (see Fig. S2 in Supporting Information). All annealed glasses were cut to the desired shape and optically polished in ethanol in six steps using SiC grinding paper (grits 220 to 4000).

2.2. Raman spectroscopy

A micro-Raman spectrometer (Renishaw inVia) equipped with a 532 nm diode pumped solid state laser was used to acquire the Raman spectra of the annealed glasses in a spectral range from 170 to 1800 cm^{-1}. All spectra were subjected to uniform background correction and area normalization.

2.3. X-ray total scattering

All scattering data were collected at the I15-1 beamline [22] at the Diamond Light Source (λ = 0.161669 Å, E = 76.69 keV). The annealed glass samples were crushed using an agate mortar and loaded into 1 mm Kapton tubes, held in place by quartz wool and finally sealed using super glue. Data of both an empty capillary and the samples were acquired in the region of Q~0.7 to 25 $Å^{-1}$, with data collected for 20 min each. The empty container measurement was subtracted, and Compton and absorption corrections were followingly applied using the GudrunX software before transforming the structure factor to the pair distribution function (in this case the differential correlation function, D(r)) [23]. The GudrunX software employs the HHS functions as described in Ref. [24] as well as a revised Lorch function for the conversion from reciprocal to real space. We refer to the GudrunX manual for a detailed introduction to this procedure [25].

2.4. Elastic properties, hardness, and crack resistance

Bulk specimens of each annealed glass were first cut into the appropriate dimensions (18 × 18 × 4 mm^3) for the ultrasonic echography and indentation measurements. The top and bottom surfaces (18 × 18 mm^2) of each glass were polished to obtain co-planar surfaces and good surface quality. Polishing was done in two steps, first using SiC grinding paper in ethanol with decreasing abrasive particle size (up to 4000 grit), and then using a water-free 1 μm diamond suspension.

The elastic properties of the glassy electrolytes were measured on these samples by means of ultrasonic echography. Specifically, the velocities of the longitudinal V_L and transversal waves V_L generated by 10 MHz piezoelectric transducers were measured. By using the following equations, Young's modulus (E) and Poisson's ratio (ν) were calculated,

$$E = \rho \frac{3V_L^2 - 4V_T^2}{\left(\frac{V_L}{V_T}\right)^2 - 1} \quad (1)$$

$$\nu = \frac{E}{2\rho V_T^2} - 1 \quad (2)$$

Here, the density (ρ) of glasses was measured by means of Archimedes' method in pure ethanol (≥99.99%) at room temperature (293.2 K).

We also performed mechanical characterization using micro-indentation (Nanovea CB500 hardness tester) to determine Vickers hardness (H_v) and crack initiation resistance (CR). Measurements were performed at room temperature (293.2 K) with a relative humidity of ~30%. To determine H_v, the glasses were indented by using a load of 0.5 N (P). The loading duration was 15 s, and dwell time was set to 10 s. At least 20 imprints were produced for each glass specimen. H_v was calculated as,

$$H_V = \frac{1.8544P}{d^2} \quad (3)$$

where d is an average of two diagonal lengths of the indents. To determine CR, i.e., the Vickers indentation load at which 50% crack probability is recorded [26], we performed a sequence of indentation tests by using a stepwise increasing load (from 0.3 to 9.8 N). The loading duration was 15 s, and dwell time was set to 10 s. At least 30 indents were produced for each glass specimen and load. The crack initiation probability is defined as the number cracks formed from the corners of a Vickers indent divided by the total number of corners.

2.5. Fracture toughness

To determine fracture toughness (K_{Ic}), we followed the experimental procedure given in ASTM standard for ceramics [27] and glasses [28,29]. That is, K_{Ic} of the glassy electrolytes was measured by means of the single-edge precracked beam (SEPB) method adopted for small dimension specimens (1.5 × 2.0 × 10 mm^3) [30]. Firstly, a line of Vickers indents with a load of 9.81 N for a dwell time of 5 s were introduced on the broadest side (B = 1.5 mm) of a polished sample beam. Then, the indented specimen was positioned in a bridge-compression fixture to produce a precrack using a cross-head speed of 0.05 mm min^{-1}. In the compression fixture, the specimen experiences tensile stress in the lower part (indented part) and compressive stress in the upper part. This allowed the controlled formation of a precrack with the size of about half-length of W to be produced. Afterwards, we used a three-point bending fixture to fracture the precracked specimen with a cross-head speed of 0.9 mm min^{-1} (to avoid the humidity effects, see Ref. [28] for details). The span (S) of 8.0 mm was designed in the adapted three-point bending according to the standard [27]. Finally, K_{Ic} was calculated from the peak load (P_{max}) [27,28,31],

$$K_{Ic} = \frac{P_{max}}{B\sqrt{W}} Y^* \quad (4)$$

$$\text{where } Y^* = \frac{3}{2}\frac{S}{W}\frac{\alpha^{1/2}}{(1-\alpha)^{3/2}} f(\alpha) \quad (5)$$

Here, Y^* is the shape factor and α is the precrack-width ratio (α/W) and $f(\alpha) = [1.99 - (\alpha - \alpha^2)(2.15 - 3.93\alpha + 2.7\alpha^2)]/(1 + 2\alpha)$. Five valid tests for each glass composition were performed to obtain an average K_{Ic} value.

2.6. MD simulation of glass formation

MD simulations of the LiBP glassy electrolytes with same compositions as those used in the experiments were performed using a GPU-accelerated [32] version of LAMMPS. A recently developed parametrization of the classical Buckingham potential from Ref. [33] was used to reproduce the structure and mechanical properties of the samples. Long-range Coulombic interactions were calculated using the particle-particle-particle-grid (PPPM) method with an accuracy of 10^{-5}.

Glass structures of the electrolytes were simulated by a melt-quenching procedure. Specifically, Li_2O, B_2O_3, and P_2O_5 units (over 9000 atoms in total) with different compositions were randomly placed in an orthorhombic box. The systems were firstly melted at 3000 K in the *NVT* ensemble for 200 ps to ensure the loss of any memory of the initial structure. Then, the systems were quenched in the *NPT* ensemble under zero pressure with a cooling rate of 1 K/ps, which helps to relieve local stresses and thus enables more accurate mechanical property simulations. Subsequentially these structures were relaxed in the *NVT* and *NPT* ensembles at 300 K for 100 ps, respectively, to generate an improved glass structure with a more accurate glass density [34]. Although the simulated density values are slightly lower than the experimental ones as shown in Table S1, this systematic difference in density has a consistent effect on the ionic conductivity estimates for all four compositions. A timestep of 1 fs was used, and Nosé-Hoover thermostat and barostat [35,36] were applied to control the temperature and pressure, respectively, when applicable.

The mean-square displacement (MSD) of Li atoms was calculated to estimate the self-diffusion coefficient D from the trajectories:

$$\text{MSD}\ (t) = \frac{1}{N}\sum_i^N [\mathbf{r}_i(0) - \mathbf{r}_i(t)]^2 \quad (6)$$

$$D = \frac{1}{6}\lim_{t\to\infty}\frac{d\langle \text{MSD}\rangle}{dt} \quad (7)$$

where N is the total number of Li atom, and $r_i(t)$ is the position vector of the ith Li atom at time t. The MSD of Li was calculated in the *NVT* ensemble at 700–800 K at an interval of 50 K to estimate the diffusion activation energy E_a by fitting an Arrhenius function to the data:

$$D = D_0 \exp(-E_a/k_B T) \quad (8)$$

where k_B is the Boltzmann constant, T is the temperature, and D_0 corresponds to the self-diffusion coefficient at infinite temperature. The calculated D values were converted to ionic conductivity (σ) at the corresponding temperature by means of the Nernst-Einstein equation:

$$\sigma = \frac{N}{V}\frac{(Ze)^2}{k_B T} D \quad (9)$$

2.7. MD simulation of elastic properties

With the assumption of isotropic structure, elastic constants were obtained by elongating the glass samples progressively in the tensile directions *xx*, *yy* and *zz* and in the shear directions *xy*, *xz* and *zy* with strain steps of ε = 0.0001 = 0.01%. After each elongation step, the structure was relaxed at 300 K for 1 ps and then simulated for another 1 ps while averaging the measured stresses in the given directions (sampled at each time step). Both procedures were conducted in the *NVT* ensemble. After recording the stress-strain curves, a linear regression was performed to obtain the elastic constants of the system. Assuming that the material system is isotropic, C_{11} and C_{44} were evaluated as the average of C_{11}, C_{22} and C_{33} and as C_{44}, C_{55} and C_{66}, respectively [37]. Based on the isotropic assumption, C_{12} was then calculated as

$$C_{12} = C_{11} - 2C_{44} \quad (10)$$

Finally, the Young's modulus (E) and Poisson's ratio (ν) were calculated by the following relations

$$E = \frac{(C_{11} - C_{12})(C_{11} + 2C_{12})}{C_{11} + C_{12}} \quad (11)$$

$$\nu = \frac{C_{12}}{C_{11} + C_{12}} \quad (12)$$

2.8. MD simulation of fracture toughness

We then used an approach developed by Brochard [38] to calculate

K_{Ic} of the simulated LiBP glassy electrolytes. In brief, simulated structures were replicated to 1 × 2 × 2 supercells, and cationic atoms were removed in an ellipse with a width of 1/3 of the longest side of the simulation box and a height of 1/5 of the width. To maintain charge neutrality, oxygens were then removed iteratively from the ellipse to match the original composition before the oxygen charge was redefined for the new composition. Such precracked samples were subjected to energy minimization followed by 1 ns of relaxation at zero pressure in the *NPT* ensemble at 300 K. The fracture experiments were initiated by equilibrating the structure for 100 ps in the *NVT* ensemble at 300 K and then gradually deforming the simulated box normal to the crack front (z-direction) using strain steps of $\varepsilon = 0.01 = 1\%$. Between each step, the structure was first minimized, then equilibrated for 5 ps, and then averaged in the strain direction by sampling the stresses at each time step for another 5 ps in the *NVT* ensemble. This sequence was repeated until a strain of 110% was reached. All the probed structures fractured completely before reaching the maximum strain. Stress-strain curves were obtained, and the critical energy release rate (G_c) was calculated by the equation:

$$G_c = \frac{L_x L_y}{\Delta A_\infty} \int_{L_{z,0}}^{L_{z,max}} \sigma_z \mathrm{d}L_z \tag{13}$$

where L designates the simulation box length, ΔA_∞ is the crack surface area obtained upon full fracture, and σ_z is the recorded stress in the z-direction. K_{Ic} values of all structures were finally calculated as,

$$K_{Ic} = \sqrt{\frac{G_c E}{1-\nu^2}} \tag{14}$$

2.9. Bond switching analysis during fracture

Deformation involves the rearrangement of atoms, which in turn occurs due to the breakage and recombination of chemical bonds during the fracture process. Consequently, the changes in atomic coordination numbers (CNs) during fracture, so-called bond switching events [39], were computed, as such events can lead to stress dissipation. We first calculated the partial pair distribution functions, where the cutoffs between M (where M represents Li, B, and P) and O were selected to be the distance at the minima after the first peak in the pair distribution function. The atoms of M and O were considered to be bonded if they were within the cutoff. The cutoffs selected in this study were 2.4 Å for Li–O pairs, 1.8 Å for B–O pairs, and 1.7 Å for P–O pairs, respectively. The bond switching analysis was then performed by comparing the CNs of each individual atom and the identity of the neighboring atom with its initial non-strained structure. If the CNs decreased or increased, then these atoms were marked as Decreased CN or Increased CN, respectively. If the neighboring atoms remain unchanged, then these atoms are labeled as Unchanged CN. Otherwise, the remaining atoms were counted as Swapped CN, indicating that the CN remained unchanged but with at least one differing neighboring atom compared to the initial state.

2.10. Rings statistic and persistent homology analysis

We used both standard ring size analysis as well as persistent homology to resolve the topological feature of rings embedded in atomic configurations produced in the MD simulations. Based on chemically bonded structures, the standard ring size analysis can identify the local ring structure where the diffusing Li atoms may be located. To this end, the structural ring size distribution was computed by the RINGS package [40], wherein a borophosphate ring is defined as the shortest closed-path within the borophosphate network excluding network-modifying Li species and terminating O atoms [41].

In the persistent homology method, the atomic positions obtained from the MD simulation are replaced by balls of a given radii according to their atomic type [42]. The size of the balls then increases (referred to as the increase of "time"). As the radii increase, two balls intersect to form an edge and some edges combine to form a closed ring, a so-called "loop", which is referred to as the "birth" time of a loop. When a ring is filled with growing balls, it is referred to as the "death" of a loop. The information obtained from loops is the one-dimensional persistence homology. The birth and death times of loops are used to make a scatter plot, the so-called persistence diagram (PD), which compiles the topological characteristics of the system. We performed the persistent homology analyses using the procedure described in Ref. [43] by using the libraries Diode [44] and Dionysus 2 [45]. We followed the approach in ref. [42] to obtain the atomic radii of $r_{Li} = 0.69$ Å, $r_B = 0.20$ Å, $r_O = 1.21$ Å and $r_P = 0.26$ Å. We then used the accumulated persistence function (APF) [43] to quantitatively compare the one-dimension PDs as,

$$\mathrm{APF}\ (t) = \sum_{i:m_i \le t} (d_i - b_i) \tag{15}$$

where b_i and d_i are the birth and death times of point i (representing a structural feature) in the PD, respectively, and $m_i = (b_i + d_i)/2$ is the mean age of point i.

3. Results and discussion

3.1. Glass structure and topology

Detailed structural information on the LiBP glassy electrolytes has been obtained through both experiments and MD simulations. Fig. 1A shows the area-normalized Raman spectra of the four glass compositions. Table S2 summarizes the band deconvolution assignment of these spectra. Distinct changes could be identified from the Raman spectra, namely the increase of fractions of $(P_2O_7)^{4-}$ and (B–O–P)$^-$ groups (band 6) and the decrease of fraction of various phosphate groups with BO_4 units (band 3) and $(PO_3)_n^{-n}$ chains (band 4) with the increase of lithium content. While keeping the relative content of B_2O_3 and P_2O_5 constant ($n(B_2O_3)/n(P_2O_5) = 1$), the introduction of lithium as a network modifier resulted in a less densified glass network structure and more $(PO_3)_n^{-n}$ chains become depolymerized, leading to an increase in the fraction of $(P_2O_7)^{4-}$ groups.

Based on the MD simulations with over 9000 atoms and periodic boundary conditions, we have reproduced the structure of LiBP glassy electrolytes, with the atomic snapshot of 38LiBP shown as an example in Fig. 1B. Fig. 1C presents the composition dependence of density as determined from experiments and MD simulations, showing a decreasing trend with increasing lithium content and a relatively small absolute differences that arises due to the higher cooling rate used in the simulations relative to the experimental melt-quenching. As such, although the densities are systematically underestimated, the trend of density with composition is well captured.

X-ray total scattering experiments were performed to measure the pair distribution function of all studied LiBP glassy electrolytes, as presented in Figs. S3 and S4. $S(q)$ and $D(r)$ are compared with the results calculated from MD simulations. An example of a direct comparison between experimental and simulated $S(q)$ and $D(r)$ is presented in Fig. 1D. Here, as well as in Fig. S3, the lack of long-range order in the LiBP glassy electrolytes is observed from the diffusive scattering of the $S(q)$ in both experiments and simulations. At the bottom of Fig. 1D, we compare the differential correlation function D(r) obtained experimentally with the results from MD simulations (38LiBP), exhibiting an overall very good agreement with R_χ value of 5.1% (metric proposed by Wright [46] to quantify the agreement between the simulated and experimental pair distribution function). This highlights the ability of the MD potential to capture the structural features of the LiBP glasses. Fig. 1E shows the partial radial distribution functions (RDF) of different pairs as calculated from the trajectory of MD simulation. The varying lithium content does not have a significant impact on the bond lengths of

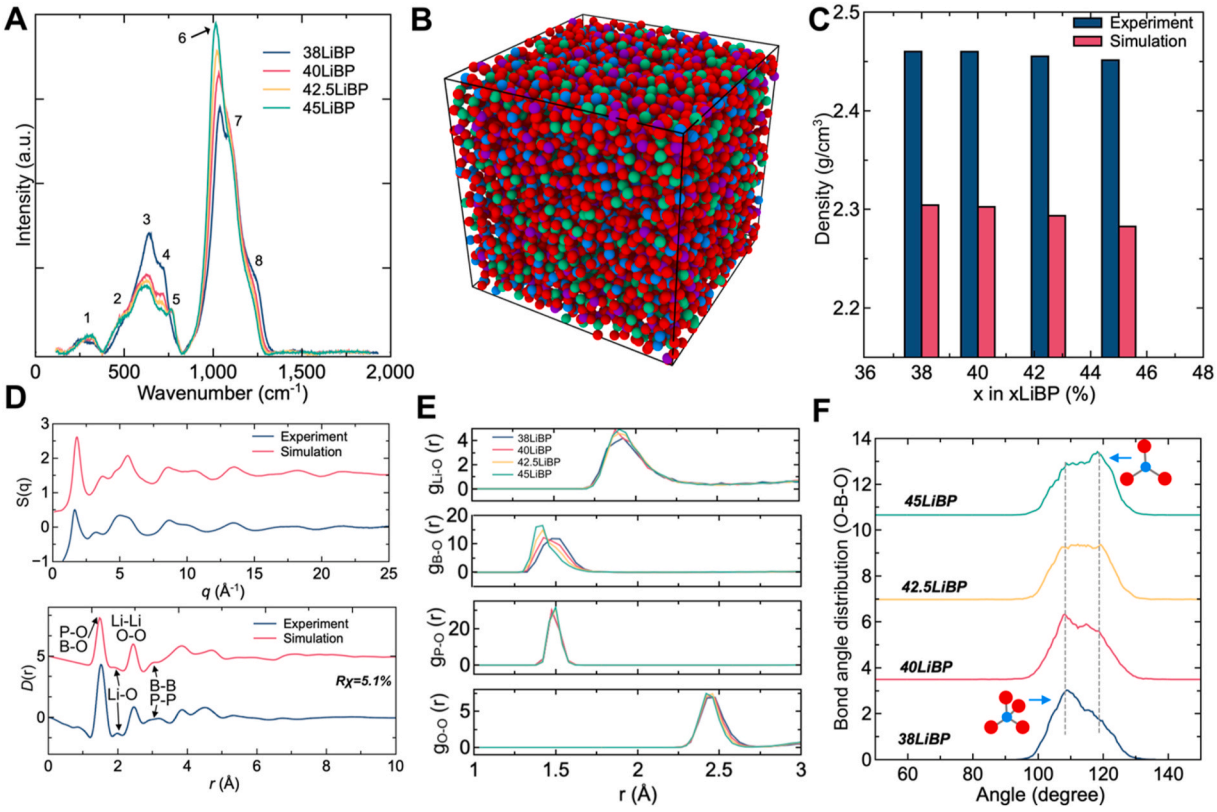

Fig. 1. (A) Raman spectra of as-prepared LiBP glassy electrolytes. The spectra were subjected to background correction and area normalization. (B) Atomic snapshot of MD-simulated 38LiBP glassy electrolytes (9720 atoms). Lithium, boron, phosphorus, and oxygen are represented by green, blue, purple, and red balls, respectively. (C) Comparison of densities of LiBP glassy electrolytes obtained from experiments and simulations. (D) Comparison between experimental (blue) and simulated (red) $S(q)$ and $D(r)$ of 38LiBP glassy electrolyte. (E) Partial radial distribution function of LiBP glassy electrolytes calculated by MD simulations. (F) Bond angle distribution of O–B–O in the simulated LiBP glassy electrolytes. (For interpretation of the references to colour in this figure legend, the reader is referred to the Web version of this article.)

Li–O, P–O and O–O, whereas we observe a decrease in the B–O bond length with higher Li content, reflecting the partial transformation of the boron coordination state from BO_4 into BO_3 units. This is also captured by the decreased CN of boron from MD simulations (see Fig. S5) and the shift of the O–B–O bond angle at ~120° as shown in Fig. 1F. Previously, the same shift from BO_4 to BO_3 with composition has been observed in NMR data of sodium borophosphate glasses [47].

3.2. Mechanical properties

Internal stresses during electrochemical cycling may lead to deformation of the solid electrolyte, hence compromising the physical contact tightness between the electrolyte and the electrode. Table S1 summarizes the composition dependence of the elastic properties of the LiBP glassy electrolytes. As the lithium content increases, the Young's modulus (E) decreases as shown by both experiments and MD simulations, i.e., the LiBP glass becomes softer. This trend is consistent with the decrease of the measured Vickers hardness (H_v). Another important aspect to enhance electrolyte lifetime is to limit the formation of cracks in the solid-state electrolytes as they hinder the transport of ions. To this end, the crack resistance (CR) is a good measure. Fig. 2A shows the load dependence of crack initiation probability of the four LiBP glassy electrolytes. Crack resistance is calculated by counting the number of indentation cracking corners. We note how challenging it is to distinguish the variation in CR with compositions especially at low loads. However, we can observe from Fig. 2A that generally the LiBP glasses appear to crack at relatively low loads, with CR around 1 N, which is lower than of most other oxide glass families [48,49]. This reflects that the LiBP glasses are very prone to cracking when subjected to high local stresses.

Once cracks appear in the solid-state electrolytes, their continued propagation will greatly hamper the performance and even leads to the failure of the solid-state battery. Such resistance of solid materials to crack propagation can be quantified by the fracture toughness, K_{Ic}, which is emerging as a determining factor for charting the performance of solid-state batteries [15]. In this work, we measured the fracture toughness of LiBP glassy electrolytes by means of the self-consistent SEPB method. Fig. S6 shows the bridge compression fixture, which was used to introduce a precrack in the sample before undergoing full fracture. Fig. 2B presents the load-displacement curves of precracked LiBP glassy electrolytes specimens during fracture. The three-point bending fixture used to fracture the samples is depicted in the top-right corner of Fig. 2B. We observe unstable fracture at P_{max}, which is required to calculate K_{Ic} based on the peak load, as it limits the stress corrosion [28]. Fig. 2C displays one post-fractured specimen of 38LiBP, with the measured precrack lengths (α) at 25%, 50%, and 75% of the broadness (B) that were applied to calculate K_{Ic} (see section 2.5 for details).

To enable interpretation of the experiments and to explore the structural changes during fracture, we also calculated the K_{Ic} values of these four different compositions of glassy electrolytes using MD simulations. The simulated fracture process is illustrated in Fig. 2D, with the region around the crack tip showing continuous bond stretching (Fig. 2D and 30% strain). This method provides stress-strain curves (Fig. 2F), which may be exploited to calculate the K_{Ic}. In the process of loading, the stress-strain curve decreases rapidly after the elastic region, i.e., LiBP glassy electrolytes show a brittle mechanical response, and the ductile region is hardly present even at the nanoscale. The calculated K_{Ic} values

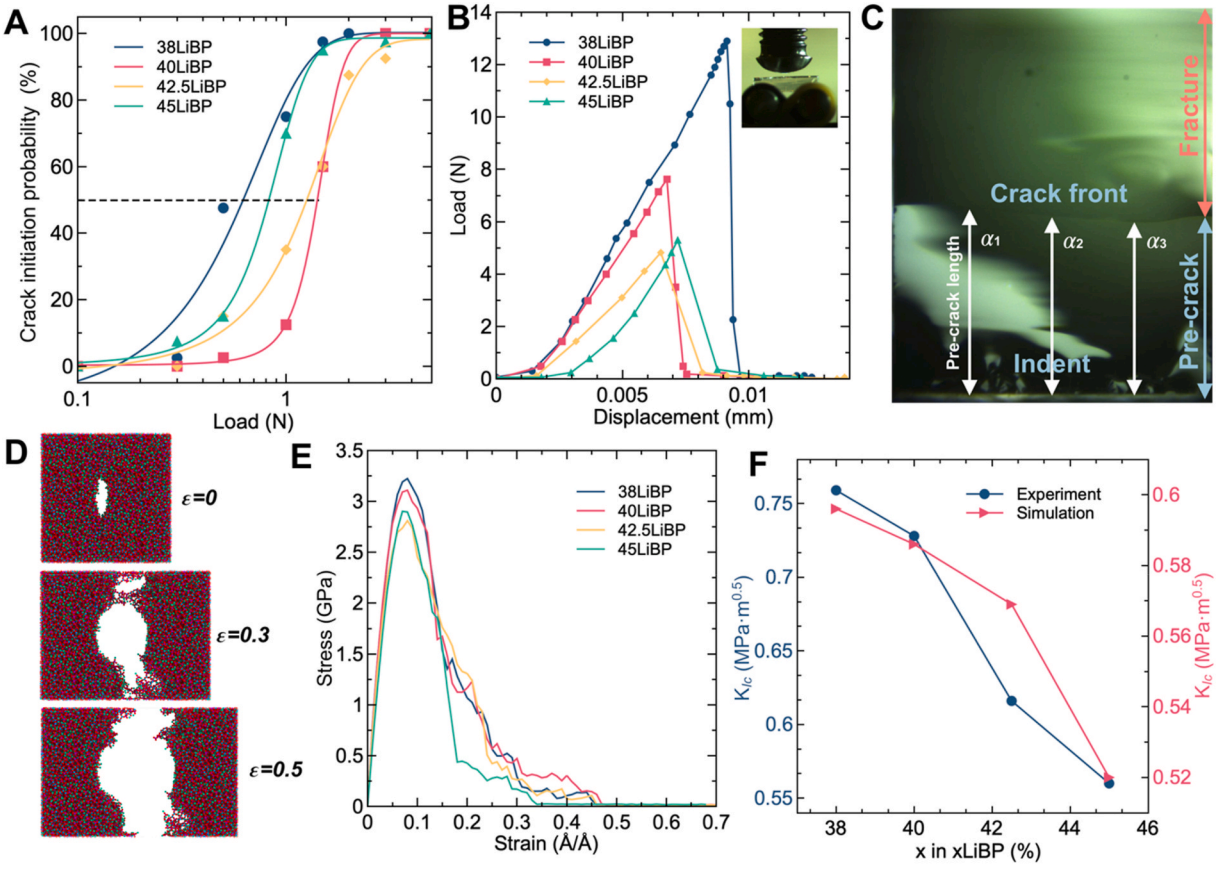

Fig. 2. (A) Crack initiation probability of LiBP glassy electrolytes. Crack resistance (CR) is determined as the load corresponding to 50% crack initial probability. (B) Load-displacement curve of three-point bending test of LiBP glasses. The top right corner is a photo of the prepared fracture specimen, taken from one of the five standard specimens of 38LiBP. (C) Example of post-fractured SEPB specimen used in the calculation of fracture toughness (K_{Ic}). (D) Atomic snapshots of simulated fracture process of LiBP glassy electrolytes at different levels of strains. Lithium, boron, phosphorus, and oxygen are represented by green, blue, purple, and red balls, respectively. (E) Stress-strain curves of LiBP glassy electrolytes calculated by MD simulations. (F) Fracture toughness (K_{Ic}) values derived from SEPB tests (calculated by Eqs. (4) and (5)) and MD simulations (calculated by Eqs. (13) and (14)). (For interpretation of the references to colour in this figure legend, the reader is referred to the Web version of this article.)

from SEPB tests and MD simulations are plotted in Fig. 2F, showing a qualitative agreement. That is, in both experiments and simulations, K_{Ic} decrease with increasing lithium content. In detail, the K_{Ic} values from SEPB tests decreases from 0.76 to 0.56 MPa $m^{0.5}$ when the lithium content increases from 38 to 45 mol%. The low fracture toughness suggests that the LiBP glassy electrolyte becomes less capable to resist crack propagation with increasing lithium content. Interestingly, the pronounced decrease in fracture toughness is observed although the change in composition is relatively small, and as such, in the following, we use MD simulations to identify the key structural changes during fracture to understand this behavior.

3.3. Bond switching during fracture

During the fracture process, energy can be dissipated by changes in chemical bonds, so-called bond switching events [39]. Bond switching events of boron have been analyzed as shown in Fig. 3. We disregard bond switching in phosphorus atoms from this analysis since no bond switching events related to phosphorus atoms occur during fracture (Fig. S7). Figs. 3 A, B, and 3C show the bond switching activities of boron atoms, which exhibit decreased, increased, and swapped CN events during the fracture process, respectively. Fig. 3D shows an atomic snapshot of the bond switching event of boron atoms under a strain of 0.1. Compared with the non-strained configurations (top three circles of Fig. 3D), the CN of the center atom boron features several possibilities apart from no change at all, i.e.: (i) the B CN may decrease from 4 to 3 (decreased CN), (ii) the B CN may increase from 3 to 4 (increased CN), and (iii) the B CN may be constant, yet with change of the identity of oxygens in its surrounding (swapped CN). The bond switching process of boron mainly relies on the CN shift from BO_3 to BO_4 in this process, accompanied by the swapping of atoms in the BO_3 and BO_4 units. Fig. 3A shows that the events of decreased CN increase sharply from the beginning of tensile process. Yet, after reaching the maximum value, the occurrence of the bond switching events decreases and levels off after the onset of fracture. Figs. 3B–C shows that the frequency of increased and swapped CN events continue to increase throughout the fracture process. After fracture, we observe some increase in the increased CN events, which can be attributed to glass relaxation, i.e., the release of stress after brittle fracture can induce some compression, leading to more increased CN and swapped CN events. This trend also agrees with the results reported in refs. [30,50]. We also observe that the fraction of atoms that exhibit bond switching events decreases as the lithium content in the LiBP glassy electrolytes increases. The drop in the fraction of atoms capable of undergoing bond switching events (and, hence, that can release stress) is the main structural origin of the decreasing fracture toughness. Based on the structural analysis of the LiBP glassy electrolytes in Figs. 1 and S8, it is noted that the CN of boron is decreasing as more lithium is incorporated in the structure, resulting in fewer possibilities to dissipate fracture energy by decreasing the CN. This may be observed from the fraction of atoms that decrease CN constitute a larger value than events associated with increased and swapped CN.

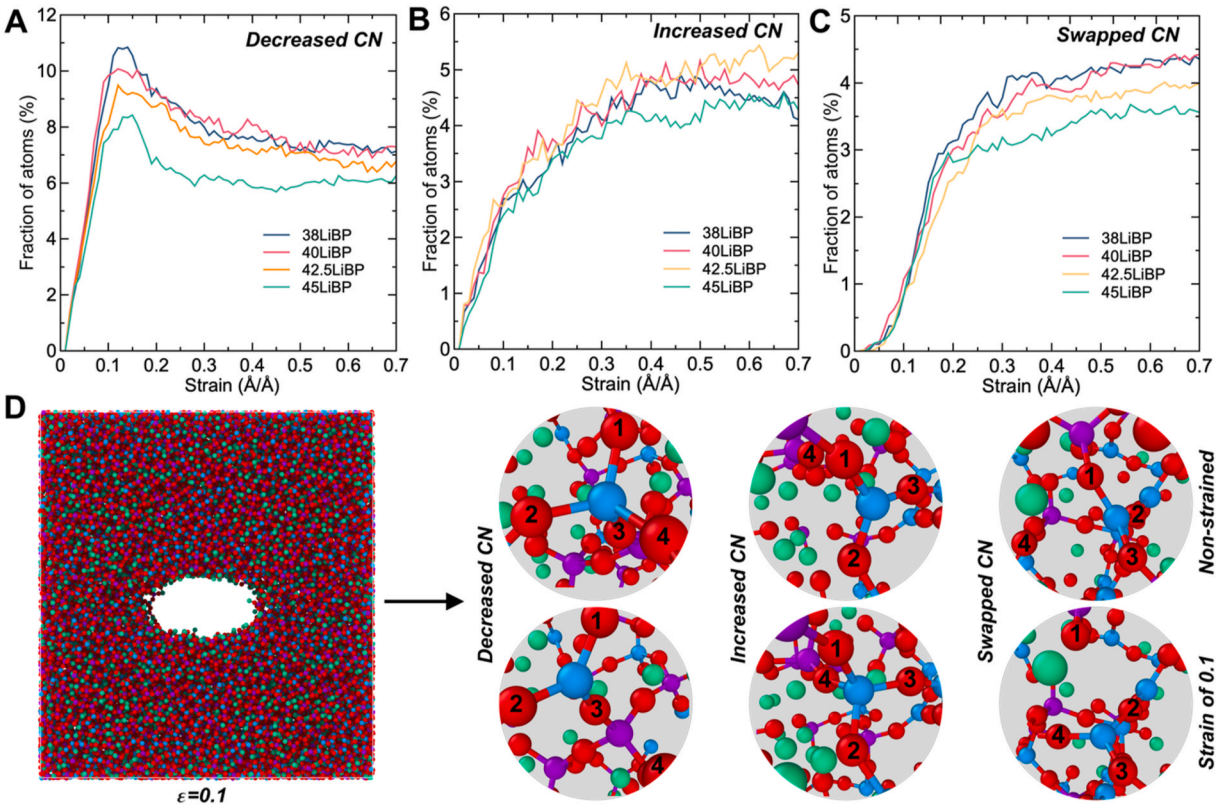

Fig. 3. Bond switching events of boron atoms during the simulated fracture process. (A) Decreased CN. (B) Increased CN. (C) Swapped CN. (D) Atomic snapshots of bond switching activities in 38LiBP glassy electrolyte at strain of 0.1. Top three circles show the non-strained atom configuration, and bottom circles are the atom configuration at a strain level of 10%. The central atom in blue is boron, green is lithium, purple is phosphorus, and red is oxygen. (For interpretation of the references to colour in this figure legend, the reader is referred to the Web version of this article.)

3.4. Ionic conductivity

Another key performance parameter of solid-state electrolytes is the ionic conductivity, which can be easily calculated from the dynamic properties of MD simulations. Hence, the mean square displacement (MSD) has been calculated to analyze the diffusion of lithium ions in the simulated glasses. The results for lithium diffusion under different temperatures are shown in Fig. S9. As exemplified in Fig. 4A, no significant diffusion of boron and phosphorus atoms has been observed. By probing the MSD at different temperatures, we find the correlation between the lithium diffusion coefficient and temperature to show an Arrhenius behavior (Fig. 4B). The results show a decrease of the activation energy of the LiBP electrolytes with an increase in the lithium content, as also previously reported experimentally [21]. The diffusion coefficient values at 300 K shown in the bottom left corner of Fig. 4B are obtained by extrapolating the high-temperature data. Further, the ionic conductivity of Li has been calculated using the Nernst-Einstein equation (Eq. (9)). As shown in Fig. S10, the increase in the calculated ionic conductivity with lithium content also coincides with that observed in experimental data reported in literature [21].

While ionic conduction in crystalline materials is generally well understood, a unified theory of conduction in the amorphous state has not yet been fully developed [19]. The diffusion path characteristics in the disordered structures are much more complex than those in crystals due to the presence of many inequivalent paths [51,52]. Although it is suggested that elemental hopping theory can still be used [15], the complex topology in the glassy electrolytes makes the extraction of lithium conduction paths much more difficult. Accordingly, we here analyze the medium-range order (MRO) structure of the LiBP glassy electrolyte using two approaches, i.e., persistent homology and ring statistical analysis to gain further insight into the structure origin of ionic conductivity [40,42,43,53]. Note that we use the same atomic configuration data (generated by MD simulations) as input for both methods. Essentially, these are two different methods used to obtain the network topology, where the ring statistical analysis considers only the topology composed by the bonded atoms, while the persistent homology method considers all the atoms in the structure (see Methods section), thereby obtaining the overall topological structure information. The results obtained by the two methods validate each other and provide interpretation of the conduction mechanism of lithium ions.

The PD shown in Fig. 4C can be used to distinguish between a range of structural features according to their loop size. Four characteristic regions can be characterized by using the invariance property with respect to the initial radius [42], i.e., the region C_T contains short-range order information from loops composed of O–P–O, whereas C_P, C_O, and B_O are characterized as MRO. By increasing the radii of the balls, the primary large loops form (marked as C_P in Fig. 4C) and each loop on C_P becomes thicker and begins to create new loops through edge contacts. These newly generated loops appear on the C_T, C_O, and B_O regions. A more detailed and rigorous mathematical definition and process for generating persistence diagrams can be found in the relevant refs. [42, 43,54]. The PDs of LiBP glassy electrolytes are quantitatively compared by following refs. [43,55], namely by calculating the APF for loops (as introduced in the method section). This method compiles the information of the PD in a simple and directly comparable manner. As shown in Fig. 4D, the APF of PDs for loops decreases with the increase of lithium content, implying that the fraction of large loops in LiBP glasses increases with lithium content.

We have also used ring statistics to analyze the topology of the LiBP glassy electrolytes. This approach considers only the chemically bonded atoms in the structure. Fig. 4E shows the ring size distributions in the LiBP glassy electrolytes, which is consistent with the persistent

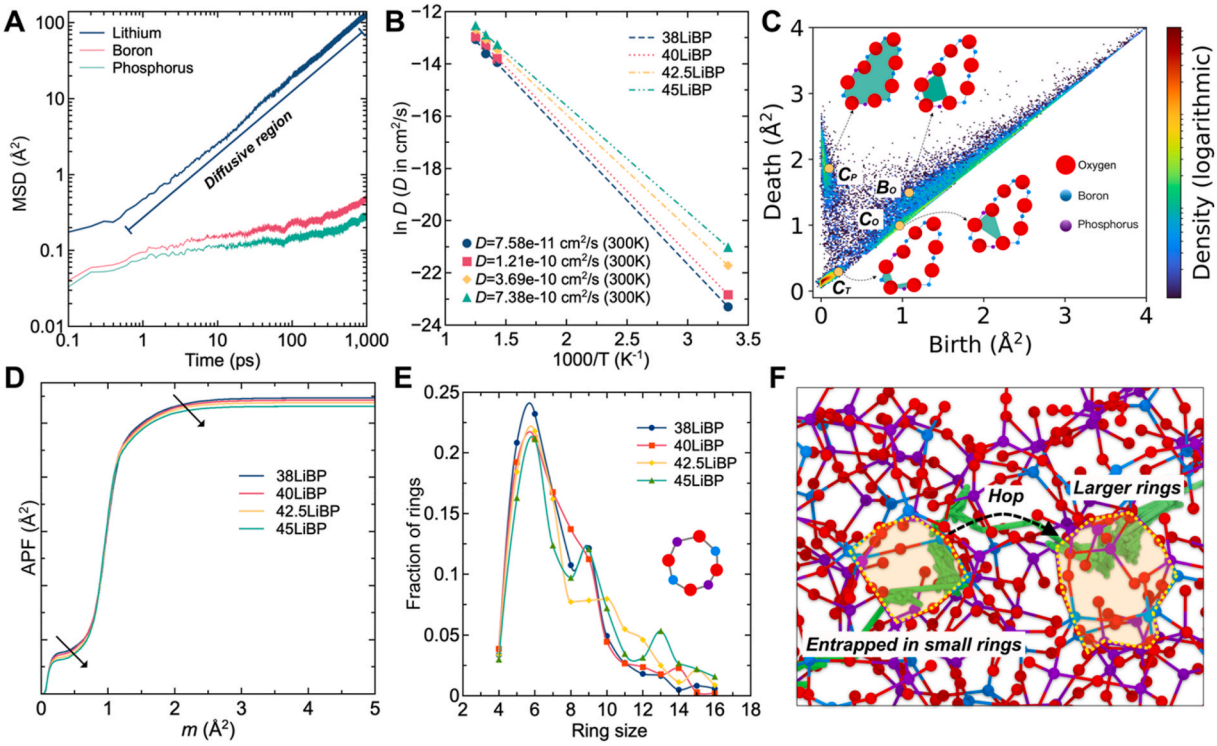

Fig. 4. (A) Mean squared displacement (MSD) in the simulated LiBP glassy electrolytes at 800 K. The lines in blue, red, and green represent the MSD of lithium, boron, and phosphorus, respectively. (B) Arrhenius fitted plot of the Li diffusion coefficient. Values at 300 K are extrapolated from the high-temperature data. (C) Persistent diagram of loops in the 38LiBP glassy electrolyte. (D) APF curves for loops as calculated from Eq. (15). The arrows represent the increase of lithium content in the LiBP glasses. (E) Ring size distribution in the simulated LiBP glassy electrolytes. (F) Schematic diagram of the migration path of a representative lithium-ion in the glass structure. The green line is the trajectory of lithium, blue is that of boron, purple is that of phosphorus, and red is that of oxygen. (For interpretation of the references to colour in this figure legend, the reader is referred to the Web version of this article.)

homology analysis. A reduction in the number of small rings and rise in the number of larger rings with increasing Li content is observed, which implies more free volume providing space for lithium diffusion. Overall, we therefore propose that variations in ring distribution associated with changing the composition of LiBP glassy electrolytes are related to the dynamic diffusion properties of lithium, as revealed by changes in the ionic conductivity. This is because we find through the MD simulations that the diffusion of lithium ions associated with small ring is more hindered, causing a tendency to jump from the small to the larger ring, as identified in Fig. 4F. The increase of the sizes of rings (loops) in the structure provides more sites for lithium to migrate and the self-diffusion coefficient of lithium increases, which is macroscopically demonstrated by the increased ionic conductivity of the glassy electrolytes.

3.5. Implications for solid-state electrolyte design

Although considerable progress has been made in the development of solid electrolytes for the application of solid-state batteries in energy storage, extensive research and development work is still needed to enable practical implementation [56]. Mechanical stability issues in particular are difficult to be overcome in the case of solid-state batteries, as complex stress changes are applied to the solid-state electrolytes [57]. Through this study, we have demonstrated the structural dependence of fracture toughness and ionic conductivity and have concluded that the rational design of solid-state electrolytes requires the disordered structure to be tuned across different length scales. First, our findings point to the important role of MRO structures on ionic conductivity. Characterizing and quantifying the MRO structure of disordered materials is challenging, but recent advances based on topological data analysis [43] and force-enhanced atomic refinement [58] could be applied to different glassy electrolyte families to further understand the relationship between ionic conductivity and the shapes and sizes of superstructural rings. To validate such simulation results, development of advanced experimental techniques for characterizing the ion transport mechanism *in operando* will be needed. Second, we have found that the fracture propensity is governed by bond switching events, as also previously observed in other glass families [30,39]. As observed herein, this suggests that elements such as boron should be incorporated in their highest coordination environment to facilitate energy dissipation. Additional work is needed to understand the relation between atomic-scale structural changes and macroscopic failure, in turn calling for *in operando* stress/strain measurements on materials with varying propensity for coordination number changes.

4. Conclusions

In this work, we investigate the atomistic origin of the variation in mechanical properties and ionic conductivity of lithium borophosphate glassy electrolytes. The fracture toughness of the glassy electrolytes has been measured by the SEPB method and thereby we have discovered that K_{Ic} decreases with increasing lithium content. Since the decrease in modulus is consistent with the variation of fracture toughness with composition, softer materials should have lower ability to resist crack formation and propagation. The fracture of glassy electrolytes can dissipate energy through bond switching events, involving both decreasing and increasing coordination number, and swapping oxygen atoms around boron atoms. We find the decreasing coordination number of boron from four to three to be the main events, which implies that the fracture toughness of LiBP electrolytes is strongly associated with the presence of BO_4 in the glass. The migration of lithium-ions in the glassy electrolytes depends on the jumps between rings, with larger rings

having more free volume to facilitate lithium-ion migration.

CRediT authorship contribution statement

Zhimin Chen: Conceptualization, Investigation, Writing – original draft. **Tao Du:** Conceptualization, Investigation, Writing – original draft. **Søren S. Sørensen:** Investigation, Writing – review & editing. **Rasmus Christensen:** Investigation, Writing – review & editing. **Qi Zhang:** Investigation, Writing – review & editing. **Lars R. Jensen:** Investigation, Writing – review & editing. **Oxana V. Magdysyuk:** Investigation, Writing – review & editing. **Maria Diaz-Lopez:** Investigation, Writing – review & editing. **Mathieu Bauchy:** Supervision, Writing – review & editing. **Yuanzheng Yue:** Supervision, Writing – review & editing. **Morten M. Smedskjaer:** Conceptualization, Supervision, Writing – original draft.

Declaration of competing interest

The authors declare that they have no known competing financial interests or personal relationships that could have appeared to influence the work reported in this paper.

Data availability

Data will be made available on request.

Acknowledgements

This work was supported by grants from China Scholarship Council (202106880010) to Z.C., Marie Skłodowska-Curie Individual Fellowship (101018156) to T.D, Independent Research Fund Denmark (1127–00003) to M.M.S, and the National Science Foundation (DMR-1928538 and 1762292) to M.B. We also thank the Diamond Light Source for access to beamline I15-1 (CY30401-1), and computational resources supplied by DeiC National HPC (DeiC-AAU-N5-202200005) and Aalborg University (CLAAUDIA).

Appendix A. Supplementary data

Supplementary data to this article can be found online at https://doi.org/10.1016/j.jpowsour.2022.232302.

References

[1] S. Chu, A. Majumdar, Opportunities and challenges for a sustainable energy future, Nature 488 (7411) (2012) 294–303, https://doi.org/10.1038/nature11475.
[2] X. Yang, X. Li, K. Adair, H. Zhang, X. Sun, Structural design of lithium-sulfur batteries: from fundamental research to practical application, Electrochem. Energy Rev. 1 (3) (2018) 239–293, https://doi.org/10.1007/s41918-018-0010-3.
[3] Y.-J. Wang, B. Fang, D. Zhang, A. Li, D.P. Wilkinson, A. Ignaszak, L. Zhang, J. Zhang, A review of carbon-composited materials as air-electrode bifunctional electrocatalysts for metal-air batteries, Electrochem. Energy Rev. 1 (1) (2018) 1–34, https://doi.org/10.1007/s41918-018-0002-3.
[4] J. Lu, Z. Chen, F. Pan, Y. Cui, K. Amine, High-performance anode materials for rechargeable lithium-ion batteries, Electrochem. Energy Rev. 1 (1) (2018) 35–53, https://doi.org/10.1007/s41918-018-0001-4.
[5] B. Scrosati, J. Hassoun, Y.-K. Sun, Lithium-ion batteries. A look into the future, Energy Environ. Sci. 4 (9) (2011) 3287–3295, https://doi.org/10.1039/C1EE01388B.
[6] H. Liu, X.-B. Cheng, J.-Q. Huang, H. Yuan, Y. Lu, C. Yan, G.-L. Zhu, R. Xu, C.-Z. Zhao, L.-P. Hou, C. He, S. Kaskel, Q. Zhang, Controlling dendrite growth in solid-state electrolytes, ACS Energy Lett. 5 (3) (2020) 833–843, https://doi.org/10.1021/acsenergylett.9b02660.
[7] M. Armand, J.-M. Tarascon, Building better batteries, Nature 451 (7179) (2008) 652–657, https://doi.org/10.1038/451652a.
[8] J.A. Dawson, P. Canepa, T. Famprikis, C. Masquelier, M.S. Islam, Atomic-scale influence of grain boundaries on Li-ion conduction in solid electrolytes for all-solid-state batteries, J. Am. Chem. Soc. 140 (1) (2018) 362–368, https://doi.org/10.1021/jacs.7b10593.
[9] J. Janek, W.G. Zeier, A solid future for battery development, Nat. Energy 1 (9) (2016), 16141, https://doi.org/10.1038/nenergy.2016.141.
[10] J.B. Goodenough, K.-S. Park, The Li-ion rechargeable battery: a perspective, J. Am. Chem. Soc. 135 (4) (2013) 1167–1176, https://doi.org/10.1021/ja3091438.
[11] J.B. Goodenough, Y. Kim, Challenges for rechargeable Li batteries, Chem. Mater. 22 (3) (2010) 587–603, https://doi.org/10.1021/cm901452z.
[12] Z. Zhang, Y. Shao, B. Lotsch, Y.-S. Hu, H. Li, J. Janek, L.F. Nazar, C.-W. Nan, J. Maier, M. Armand, L. Chen, New horizons for inorganic solid state ion conductors, Energy Environ. Sci. 11 (8) (2018) 1945–1976, https://doi.org/10.1039/C8EE01053F.
[13] L. Porz, T. Swamy, B.W. Sheldon, D. Rettenwander, T. Frömling, H.L. Thaman, S. Berendts, R. Uecker, W.C. Carter, Y.-M. Chiang, Mechanism of lithium metal penetration through inorganic solid electrolytes, Adv. Energy Mater. 7 (20) (2017), 1701003, https://doi.org/10.1002/aenm.201701003.
[14] R. Koerver, W. Zhang, L. de Biasi, S. Schweidler, A.O. Kondrakov, S. Kolling, T. Brezesinski, P. Hartmann, W.G. Zeier, J. Janek, Chemo-mechanical expansion of lithium electrode materials - on the route to mechanically optimized all-solid-state batteries, Energy Environ. Sci. 11 (8) (2018) 2142–2158, https://doi.org/10.1039/C8EE00907D.
[15] T. Famprikis, P. Canepa, J.A. Dawson, M.S. Islam, C. Masquelier, Fundamentals of inorganic solid-state electrolytes for batteries, Nat. Mater. 18 (12) (2019) 1278–1291, https://doi.org/10.1038/s41563-019-0431-3.
[16] V. Viallet, V. Seznec, A. Hayashi, M. Tatsumisago, A. Pradel, Glasses and glass-ceramics for solid-state battery applications, in: J.D. Musgraves, J. Hu, L. Calvez (Eds.), Springer Handbook of Glass, Springer Handbooks, Springer International Publishing, Cham, 2019, pp. 1697–1754, https://doi.org/10.1007/978-3-319-93728-1_50.
[17] K.E. Aifantis, J.P. Dempsey, Stable crack growth in nanostructured Li-batteries, J. Power Sources 143 (1) (2005) 203–211, https://doi.org/10.1016/j.jpowsour.2004.11.037.
[18] C.E. Athanasiou, X. Liu, M.Y. Jin, E. Nimon, S. Visco, C. Lee, M. Park, J. Yun, N. P. Padture, H. Gao, B.W. Sheldon, Rate-dependent deformation of amorphous sulfide glass electrolytes for solid-state batteries, Cell Rep. Phys. Sci. 3 (4) (2022), 100845, https://doi.org/10.1016/j.xcrp.2022.100845.
[19] A. Chandra, A. Bhatt, A. Chandra, Ion conduction in superionic glassy electrolytes: an overview, J. Mater. Sci. Technol. 29 (3) (2013) 193–208, https://doi.org/10.1016/j.jmst.2013.01.005.
[20] A. Bunde, K. Funke, M.D. Ingram, Ionic glasses: history and challenges, Solid State Ionics 105 (1) (1998) 1–13, https://doi.org/10.1016/S0167-2738(97)00444-X.
[21] K.I. Cho, S.H. Lee, K.H. Cho, D.W. Shin, Y.K. Sun, Li2O–B2O3–P2O5 solid electrolyte for thin film batteries, J. Power Sources 163 (1) (2006) 223–228, https://doi.org/10.1016/j.jpowsour.2006.02.011.
[22] XPDF (I15-1), Diamond Light Source. https://www.diamond.ac.uk/Instruments/Crystallography/I15-1.html#. (Accessed 14 August 2022).
[23] A.K. Soper, E.R. Barney, Extracting the pair distribution function from white-beam X-ray total scattering data, J. Appl. Crystallogr. 44 (4) (2011) 714–726, https://doi.org/10.1107/S0021889811021455.
[24] D.A.A. Keen, Comparison of various commonly used correlation functions for describing total scattering, J. Appl. Crystallogr. 34 (2) (2001) 172–177, https://doi.org/10.1107/S0021889800019993.
[25] A. Soper, GudrunN and GudrunX: programs for correcting raw neutron and X-ray diffraction data to differential scattering cross section, Rutherford Appleton Laboratory Tech.Rep.RAL-TR-2011-013 (2011).
[26] K. Januchta, R.E. Youngman, A. Goel, M. Bauchy, S.L. Logunov, S.J. Rzoska, M. Bockowski, L.R. Jensen, M.M. Smedskjaer, Discovery of ultra-crack-resistant oxide glasses with adaptive networks, Chem. Mater. 29 (14) (2017) 5865–5876, https://doi.org/10.1021/acs.chemmater.7b00921.
[27] C28 Committee. Standard Test Methods for Determination of Fracture Toughness of Advanced Ceramics at Ambient Temperature; ASTM International. https://doi.org/10.1520/C1421-10.
[28] T. To, F. Célarié, C. Roux-Langlois, A. Bazin, Y. Gueguen, H. Orain, M. Le Fur, V. Burgaud, T. Rouxel, Fracture toughness, fracture energy and slow crack growth of glass as investigated by the single-edge precracked beam (SEPB) and chevron-notched beam (CNB) methods, Acta Mater. 146 (2018) 1–11, https://doi.org/10.1016/j.actamat.2017.11.056.
[29] K. Januchta, T. To, M.S. Bødker, T. Rouxel, M.M. Smedskjaer, Elasticity, hardness, and fracture toughness of sodium aluminoborosilicate glasses, J. Am. Ceram. Soc. 102 (8) (2019) 4520–4537, https://doi.org/10.1111/jace.16304.
[30] T. To, S.S. Sørensen, J.F.S. Christensen, R. Christensen, L.R. Jensen, M. Bockowski, M. Bauchy, M.M. Smedskjaer, Bond switching in densified oxide glass enables record-high fracture toughness, ACS Appl. Mater. Interfaces 13 (15) (2021) 17753–17765, https://doi.org/10.1021/acsami.1c00435.
[31] J.E. Srawley, Wide range stress intensity factor expressions for ASTM E 399 standard fracture toughness specimens, Int. J. Fract. 12 (3) (1976) 475–476, https://doi.org/10.1007/BF00032844.
[32] W.M. Brown, P. Wang, S.J. Plimpton, A.N. Tharrington, Implementing molecular dynamics on hybrid high performance computers – short range forces, Comput. Phys. Commun. 182 (4) (2011) 898–911, https://doi.org/10.1016/j.cpc.2010.12.021.
[33] L. Deng, J. Du, Development of boron oxide potentials for computer simulations of multicomponent oxide glasses, J. Am. Ceram. Soc. 102 (5) (2019) 2482–2505, https://doi.org/10.1111/jace.16082.
[34] S. Sundararaman, L. Huang, S. Ispas, W. Kob, New interaction potentials for borate glasses with mixed network formers, J. Chem. Phys. 152 (10) (2020), 104501, https://doi.org/10.1063/1.5142605.
[35] S. Nosé, A unified formulation of the constant temperature molecular dynamics methods, J. Chem. Phys. 81 (1) (1984) 511–519, https://doi.org/10.1063/1.447334.

[36] W.G. Hoover, Canonical dynamics: equilibrium phase-space distributions, Phys. Rev. A 31 (3) (1985) 1695–1697, https://doi.org/10.1103/PhysRevA.31.1695.
[37] J.I. Gersten, F.W. Smith, The Physics and Chemistry of Materials, Wiley, New York, 2001.
[38] L. Brochard, G. Hantal, H. Laubie, F.J. Ulm, R.J.-M. Pellenq, Fracture mechanisms in organic-rich shales: role of Kerogen, Poromechanics V Proc. Fifth Biot Conf. Poromechanics (2013) 2471–2480, https://doi.org/10.1061/9780784412992.288.
[39] E.J. Frankberg, J. Kalikka, F. García Ferré, L. Joly-Pottuz, T. Salminen, J. Hintikka, M. Hokka, S. Koneti, T. Douillard, B. Le Saint, P. Kreiml, M.J. Cordill, T. Epicier, D. Stauffer, M. Vanazzi, L. Roiban, J. Akola, F. Di Fonzo, E. Levänen, K. Masenelli-Varlot, Highly ductile amorphous oxide at room temperature and high strain rate, Science 366 (6467) (2019) 864–869, https://doi.org/10.1126/science.aav1254.
[40] S. Le Roux, P. Jund, Ring statistics analysis of topological networks: new approach and application to amorphous GeS2 and SiO2 systems, Comput. Mater. Sci. 49 (1) (2010) 70–83, https://doi.org/10.1016/j.commatsci.2010.04.023.
[41] L. Guttman, Ring structure of the crystalline and amorphous forms of silicon dioxide, J. Non-Cryst. Solids 116 (2) (1990) 145–147, https://doi.org/10.1016/0022-3093(90)90686-G.
[42] Y. Hiraoka, T. Nakamura, A. Hirata, E.G. Escolar, K. Matsue, Y. Nishiura, Hierarchical structures of amorphous solids characterized by persistent homology, Proc. Natl. Acad. Sci. USA 113 (26) (2016) 7035–7040, https://doi.org/10.1073/pnas.1520877113.
[43] S.S. Sørensen, C.A.N. Biscio, M. Bauchy, L. Fajstrup, M.M. Smedskjaer, Revealing hidden medium-range order in amorphous materials using topological data analysis, Sci. Adv. 6 (37) (2020) eabc2320, https://doi.org/10.1126/sciadv.abc2320.
[44] Diode. https://Github.Com/Mrzv/Diode.
[45] Dionysus2. https://Mrzv.Org/Software/Dionysus2/.
[46] A.C. Wright, The comparison of molecular dynamics simulations with diffraction experiments, J. Non-Cryst. Solids 159 (3) (1993) 264–268, https://doi.org/10.1016/0022-3093(93)90232-M.
[47] C. Hermansen, R.E. Youngman, J. Wang, Y. Yue, Structural and topological aspects of borophosphate glasses and their relation to physical properties, J. Chem. Phys. 142 (18) (2015), 184503, https://doi.org/10.1063/1.4919798.
[48] Y. Kato, H. Yamazaki, S. Yoshida, J. Matsuoka, Effect of densification on crack initiation under Vickers indentation test, J. Non-Cryst. Solids 356 (35) (2010) 1768–1773, https://doi.org/10.1016/j.jnoncrysol.2010.07.015.
[49] T. To, L.R. Jensen, M.M. Smedskjaer, On the relation between fracture toughness and crack resistance in oxide glasses, J. Non-Cryst. Solids 534 (2020), 119946, https://doi.org/10.1016/j.jnoncrysol.2020.119946.
[50] T. Du, H. Liu, L. Tang, S.S. Sørensen, M. Bauchy, M.M. Smedskjaer, Predicting fracture propensity in amorphous alumina from its static structure using machine learning, ACS Nano 15 (11) (2021) 17705–17716, https://doi.org/10.1021/acsnano.1c05619.
[51] W. Li, Y. Ando, E. Minamitani, S. Watanabe, Study of Li atom diffusion in amorphous Li3PO4 with neural network potential, J. Chem. Phys. 147 (21) (2017), 214106, https://doi.org/10.1063/1.4997242.
[52] S. Adams, J. Swenson, Bond valence analysis of reverse Monte Carlo produced structural models; a way to understand ion conduction in glasses, J. Phys. Condens. Matter 17 (5) (2005) S87–S101, https://doi.org/10.1088/0953-8984/17/5/010.
[53] T. Du, H. Li, Q. Zhou, Z. Wang, G. Sant, J.V. Ryan, M. Bauchy, Atomistic origin of the passivation effect in hydrated silicate glasses, Npj Mater. Degrad. 3 (1) (2019) 1–7, https://doi.org/10.1038/s41529-019-0070-9.
[54] H. Edelsbrunner, J.L. Harer, Computational Topology: an Introduction, American Mathematical Society, 2010.
[55] C.A.N. Biscio, J. Møller, The accumulated persistence function, a new useful functional summary statistic for topological data analysis, with a view to brain artery trees and spatial point process applications, J. Comput. Graph Stat. 28 (3) (2019) 671–681, https://doi.org/10.1080/10618600.2019.1573686.
[56] A. Manthiram, X. Yu, S. Wang, Lithium battery chemistries enabled by solid-state electrolytes, Nat. Rev. Mater. 2 (4) (2017) 1–16, https://doi.org/10.1038/natrevmats.2016.103.
[57] L.R. Mangani, C. Villevieille, Mechanical *vs.* Chemical stability of sulphide-based solid-state batteries. Which one is the biggest challenge to tackle? Overview of solid-state batteries and hybrid solid state batteries, J. Mater. Chem. 8 (20) (2020) 10150–10167, https://doi.org/10.1039/D0TA02984J.
[58] Q. Zhou, Y. Shi, B. Deng, J. Neuefeind, M. Bauchy, Experimental method to quantify the ring size distribution in silicate glasses and simulation validation thereof, Sci. Adv. 7 (28) (2021) eabh1761, https://doi.org/10.1126/sciadv.abh1761.